Journal of Civil Engineering and Urban Planning (2026)
Clausius Scientific Press, Canada

DOI: 10.23977/jceup.2026.080109
ISSN 2616-3969 Vol. 8 Num. 1

Experimental Study on the Uniaxial Compressive Stress-strain Behavior of Alkali-activated Slag/Fly Ash-based All Fly Ash Aggregate Concrete

Chenxi Zhao

College of Architecture and Civil Engineering, Beijing University of Technology, Beijing, 100124, China

Keywords: Alkali activated slag fly ash concrete; Fly ash lightweight aggregate; Uniaxial compression test; Stress-strain curve; Normalization

Abstract: To promote the engineering application of fully solid waste-based low-carbon concrete, the uniaxial compression behavior of a novel alkali-activated slag/fly ash-based all fly ash aggregate concrete (AASF-AFAAC) was investigated. Thirty cylindrical specimens divided into five groups with varying fly ash contents were prepared for uniaxial compression tests. Based on normalized stress-strain curves, the experimental results were fitted and analyzed using the Guo Zhenhai model. The results indicate that the Guo Zhenhai model achieved the highest fitting accuracy and effectively described the nonlinear mechanical behavior of the material during compression. This study provides reliable mechanical model support for the structural analysis and engineering application of fully solid waste-based alkali-activated lightweight aggregate concrete, achieving the goal of identifying the optimal fitting method.

1. Introduction

China's urbanization continues to advance, driving a surge in demand for natural sand and gravel. By 2024, national consumption exceeded 18 billion tons, with over 70% sourced from natural extraction [1,2]. Long-term large-scale mining has led to resource depletion and supply instability, resulting in aggregate shortages in one-third of provinces by 2018 [3], making the development of alternative resources imperative. Meanwhile, China emits approximately 800 million tons of fly ash annually. Although the comprehensive utilization rate reaches 68%-70%, over 50 million tons remain buried in landfills [4], posing severe environmental risks. High-value utilization of fly ash is crucial for resource conservation and sustainable environmental development.

To address the aforementioned challenges, constructing lightweight high-performance concrete systems by using artificial lightweight aggregates such as fly ash aerogels (SFA) and fly ash spherules (FAC) as substitutes for natural aggregates represents a crucial direction in resource recycling. These materials exhibit characteristics including low density, high specific strength, and thermal insulation properties, and have been widely applied in replacing natural aggregates for lightweight concrete (LWAC) production [5-8]. Early research on fly ash aerogel-based lightweight concrete (SFA-LWAC) focused on mechanical properties: Kayali et al. demonstrated that fly ash

aerogels can be used to prepare lightweight high-strength concrete, though their elastic modulus remains lower than that of conventional concrete [9]. Regarding durability, Domagała's studies showed that SFA-LWAC exhibits comparable or even superior water permeability resistance and freeze-thaw performance compared to ordinary concrete [10]. Research on fly ash spherule-based lightweight concrete (FAC-LWAC) has also reached maturity: Patel's FAC-LWAC achieved strength comparable to conventional concrete [11]; Guo Jia et al. found that fly ash spherules significantly improve concrete workability, but high substitution rates compromise mechanical properties [12]; further studies revealed that fly ash spherules enhance concrete resistance to chloride ion penetration, dimensional stability [13], and fire resistance [14].

In the aforementioned studies, both SFA-LWAC and FAC-LWAC utilized cement as the binding material, which poses significant environmental pollution risks due to cement production. China's cement manufacturing industry emits approximately 1.1 billion tons of CO_2 annually, accounting for 13% of the nation's total emissions [15]. To reduce carbon emissions, some researchers have proposed alkali slag concrete (AASC). Life cycle studies indicate that compared to conventional Portland cement concrete, AASC can reduce greenhouse gas emissions by 44%-64% while lowering costs by 7%-39% [16-17]. Additionally, AASC exhibits advantages such as low water demand, minimal hydration heat, and superior mechanical and durability properties (e.g., resistance to chloride ion penetration, frost damage, and fire resistance) [18-20]. However, the excessively rapid reaction rate in alkali slag systems results in extremely short setting times and high shrinkage rates, limiting large-scale application of AASC [21]. Existing research demonstrates that incorporating fly ash into alkali slag concrete more effectively reduces self-shrinkage and drying shrinkage compared to pure slag systems [22].

Building upon the aforementioned research, this paper proposes a novel alkali-activated slag/powdered fly ash-based all-fly ash aggregate concrete (AASF-AFAAC). The material employs powdered fly ash ceramsite (SFA) as a substitute for natural coarse aggregates, utilizes powdered fly ash silted beads (FAC) as a replacement for natural fine aggregates, and adopts alkali-activated slag/powdered fly ash composite cementitious materials to replace conventional cement.

Previous studies have systematically investigated the mechanical properties of AASF-AFAAC. In subsequent chapters, with fly ash content as the primary variable, uniaxial compression tests were conducted on 30 cylindrical AASF-AFAAC specimens. Stress-strain curves were analyzed to qualitatively examine the influence of fly ash content on elastic modulus and peak strain. Additionally, based on existing concrete constitutive models, a modified stress-strain relationship tailored for AASF-AFAAC was proposed, aiming to provide reliable theoretical foundations for nonlinear analysis and engineering applications of AASF-AFAAC structures.

2. Overview of the Trial

2.1 Experimental Design

This study prepared 30 cylindrical specimens with dimensions of Φ150mm × 300mm. The fly ash content was defined as the mass percentage of fly ash replacing slag. Based on prior research [23,24], five substitution levels (0%,10%,20%,30%, and 40%) were selected. The mix design was formulated in accordance with the "Code for Design of Mix Proportions for Ordinary Concrete" (JGJ 55-2011) [25]. Detailed mix composition is presented in Table 1.

Table 1: Mix proportion design for AASF-AFAAC

Sample group	flyash /(kg/m3)	slag/(kg/m3)	Fly ash sedimentation beads/(kg/m3)	Fly ash ceramsite/(kg/m3)
AASF-AFAAC0	0	600	262.5	500
AASF-AFAAC10	60	540	262.5	500
AASF-AFAAC20	120	480	262.5	500
AASF-AFAAC30	180	420	262.5	500
AASF-AFAAC40	240	360	262.5	500

2.2 Test Materials

Granulated blast furnace slag (GBFS) and Class I fly ash were provided by Longze Water Purification Materials Co., Ltd. in Gongyi City, China, with their chemical compositions summarized in Table 2 and Table 3, respectively. Fly ash silted beads (FAC) used as fine aggregate were purchased from Henan Zhengzhou Hengyuan New Materials Co., Ltd., with their basic physical properties and morphology presented in Table 4 and Figure 1(a), respectively. Fly ash ceramsite (SFA) serving as coarse aggregate was supplied by Anhui Kongshi Environmental Protection Technology Co., Ltd., with its physical properties measured according to the Technical Specification for Lightweight Aggregate Concrete (JGJ 51-2002) [26] summarized in Table 5, and representative SFA particles displayed in Figure 1(b).

Table 2: Chemical composition of GBFS

ingredient	SiO_2	Al_2O_3	MgO	Fe_2O_3	else
content /%	34.50	17.70	6.01	1.03	6.76

Table 3: Chemical composition of Class I fly ash

ingredient	SiO_2	Al_2O_3	CaO	Fe_2O_3	SO_3	else
content /%	49.26	30.14	6.53	5.16	2.16	6.75

Table 4: Product information of FAC

product name	shape of product	product appearance	loss on ignition	fineness
Fly ash sedimentation beads	powder-like	Gray/White	≤ 1.5	20-3000 mesh

(a) Fly ash sedimentation beads (b) Fly ash ceramsite

Figure 1: Fly ash aggregate

Table 5: Physical properties of SFA

Aggregate type	Bulk density / (kg/m ^{3})	Density level	Cylinder compressive strength / MPa	1 h water absorption rate/%	coefficient of softing	Mud content/%	Boiling loss rate/%
FAC	650	877	12.1	11.0	0.85	1.6	2.4

The alkali activator consists of liquid NaSiO3 and NaOH particles. The liquid sodium silicate contains 29.99% SiO2, 13.75% Na2O, and 56.26% water content, with a modulus of 2.25. The solid sodium hydroxide has a purity of 96%. This study maintains a fixed water glass dosage of 15% and an activator mixture solution modulus of 1.2. The composition of liquid sodium silicate and solid sodium hydroxide is illustrated in Figure 2.

(a) mineral adhesive (b) Sodium hydroxide particles

Figure 2: Raw materials of alkali-activated activator

2.3 Concrete Preparation and Testing Methods

First, moisten the mixing equipment to minimize water absorption by lightweight aggregates. Stir coarse and fine aggregates with partial water at low speed for 60 seconds until fully hydrated. Add cementitious materials such as slag and fly ash, then mix for 60 seconds to ensure solid component dispersion. Next, incorporate alkali-activated solution, superplasticizer, and residual water, stirring for 60 seconds to form a homogeneous slurry. After mold placement, compact the mixture for 30 seconds to eliminate air bubbles, followed by 24-hour static curing. Demold the specimen and store it in a sealed environment at 20±1°C with relative humidity ≥95% until testing.

Figure 3 illustrates the experimental setup for measuring axial compressive strength and elastic modulus. The cylindrical compressive strength test employs force-controlled loading with a preset loading rate of 0.88 kN/s. For the elastic modulus test, force-controlled loading is applied at the same rate, maintaining a load of 0.5 MPa for 60 seconds while collecting strain data over 30 seconds. After reaching one-third of the compressive strength threshold, the loading and holding procedure is repeated. If the relative deformation deviation at any measurement point exceeds 20%, the test must be repeated at least twice.

(a) Testing facility

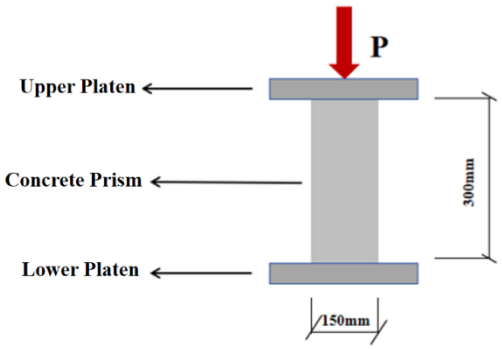

(b) Diagrammatic sketch

Figure 3 Axial compression test of AASF-AFAAC

3. Experimental Results and Analysis

3.1 ASF-AFAAC Stress-Strain Relationship Curve

Three specimens of each AASF-AFAAC group underwent cylindrical compression tests to collect load-displacement curve data. After excluding abnormal test values, the collected data was analyzed to derive the AASF-AFAAC stress-strain curves as shown in Figure 4. It should be noted that due to the specimens' pronounced brittleness during compression and the limited rigidity of the testing equipment, stable loading and data acquisition proved challenging in the post-peak phase. Consequently, this study primarily obtained the ascending segment of the stress-strain curves.

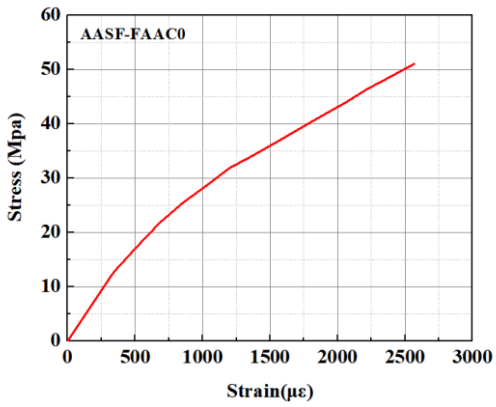

(a)AASF-AFAAC0

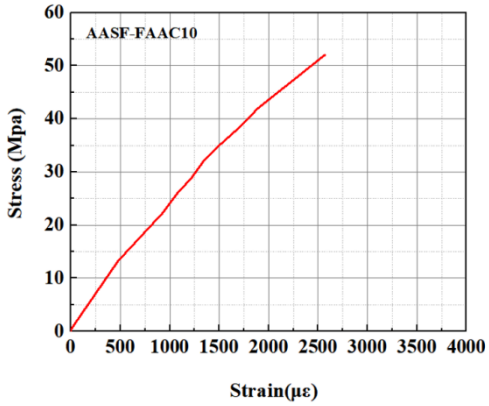

(b)AASF-AFAAC10

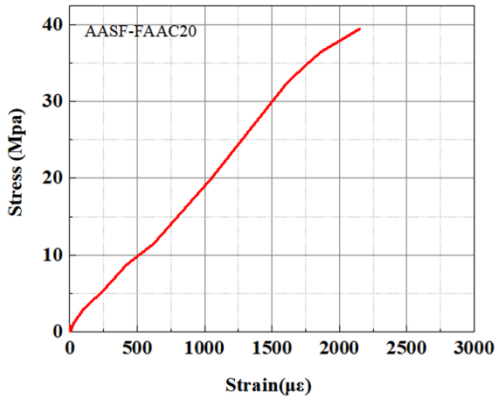

(c)AASF-AFAAC20

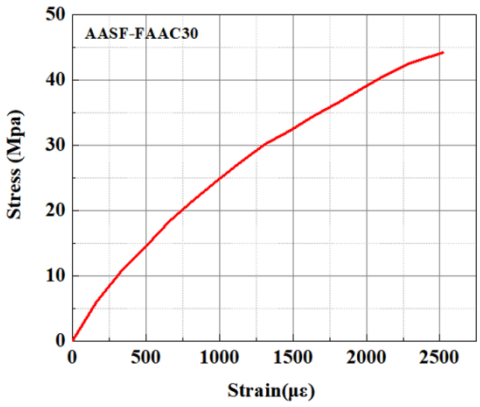

(d)AASF-AFAAC30

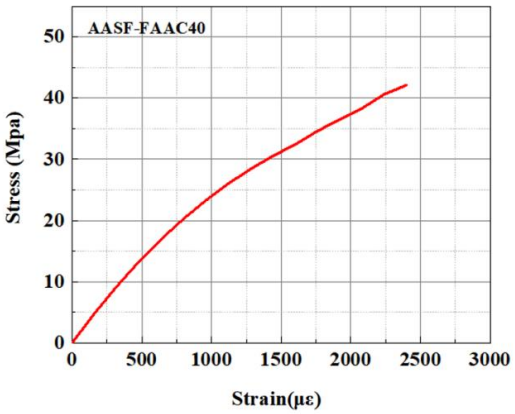

(e)AASF-AFAAC40

Figure 4: Stress-Strain Curve of AASF-AFAAC

The stress-strain curves of AASF-AFAAC0-AASF-AFAAC40 were plotted together for comparison in Figure 5, followed by a qualitative analysis of how fly ash content affects key parameters including compressive strength, elastic modulus, and peak strain of the AASF-AFAAC cylindrical specimens.

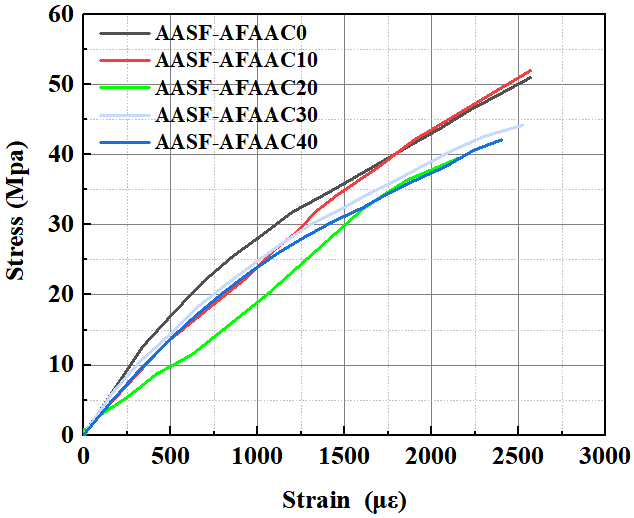

Figure 5: AASF-AFAAC compression σ-ε curve

As shown in Figure 5, the compressive strength of cylindrical specimens exhibits a "initial decline → subsequent recovery → stabilization" pattern with increasing fly ash content, with the lowest strength observed in the AASF-AFAAC20 group. At low dosages (0-10%), reactive SiO_2 and Al_2O_3 in fly ash participate in alkali-induced reactions to form N-A-S-H gels, while micro-particles fill pores and enhance matrix density, resulting in stable strength. At 20% dosage, diluted calcium sources lead to incomplete fly ash reactions, reduced gel formation, and increased porosity, causing a sharp strength drop. At 30% dosage, enhanced micro-packing effects and potential volcanic ash reactions improve matrix structure, allowing strength recovery. However, at 40% dosage, insufficient reactive components generate weak interfaces from unreacted particles, introduce defects, and reduce material continuity, leading to further strength decline. Notably, compressive strength sensitivity to internal defects and structural uniformity becomes more pronounced at higher dosages. Moderate fly ash incorporation improves microstructure and maintains strength through filling effects and potential reactions, whereas excessive dosage adversely affects compressive

performance due to insufficient reactions and increased pore defects[28-29].

The tangent slope at the origin of the stress-strain curve corresponds to the elastic modulus of concrete. Analysis of initial slope variations across test groups reveals that this parameter serves as a key indicator of concrete's elastic properties. Notably, the elastic modulus exhibits a characteristic pattern: initially remaining stable with increasing fly ash content before gradually declining. This behavior primarily stems from fly ash's reactive nature within alkali-activated systems and its impact on matrix density. At lower dosages, fly ash dissolves in alkaline environments to form N-A-S-H or C-A-S-H gels that fill mortar voids, enhancing matrix compactness and resulting in minimal modulus changes. However, increased fly ash content leads to reduced cementitious products due to lower reactivity compared to slag. This diminishes matrix continuity, elevates porosity, and decreases overall stiffness, ultimately causing modulus reduction. Additionally, the smooth spherical surface of fly ash weakens aggregate-cement matrix adhesion, creating porous transition zones that further compromise compressive deformation resistance. Consequently, a significant modulus drop becomes evident at 40% fly ash content[30-32].

Comparative analysis of peak compressive strain across test specimens reveals that with increasing fly ash content, the AASF-AFAAC composite exhibits a "initial significant decrease → subsequent recovery → further decline" strain pattern. This behavior correlates closely with fly ash's reactive characteristics in alkali-activated systems and its microstructural regulatory effects. Specifically: At zero or low fly ash content, the system maintains high slag proportion, abundant C-A-S-H gel formation, excellent matrix continuity, and high compressive deformation capacity, resulting in elevated peak strain. When content increases to 10%-20%, diluted active slag proportion reduces reaction intensity and gel production, while incomplete fly ash particle reaction compromises matrix density and material deformation capability, leading to significant strain reduction. At 30% content, enhanced fine particle filling effects and latent volcanic ash reactions partially offset slag reduction's negative impact, optimizing matrix porosity structure and restoring deformation capacity, which triggers strain recovery. However, at 40% content, insufficient active calcium sources prevent effective fly ash activation, causing unreacted particles to form weak interfaces and increased pore defects that facilitate crack initiation and propagation during loading, resulting in renewed strain reduction.

The normalized stress-strain raw data obtained from the experiment were processed, with the dimensionless curve's ascending phase illustrated in Figure 6. Analysis of the normalized curve morphology reveals that the stress-strain relationship under axial compression can be broadly categorized into three stages: initial compaction phase, elastic phase, and nonlinear ascending phase. During the initial loading stage, stress growth remains relatively slow, primarily reflecting the gradual compaction of internal pores and interfacial defects within the specimen. As strain increases, the material enters an approximately linear elastic phase where stress-strain relationships exhibit near-linearity, indicating stable overall structural integrity. When strain continues to rise, the curve gradually deviates from linear behavior and enters the nonlinear phase, during which micro-cracks begin to form and propagate within the material. Nevertheless, the overall load-bearing capacity maintains consistent growth until peak stress is achieved.

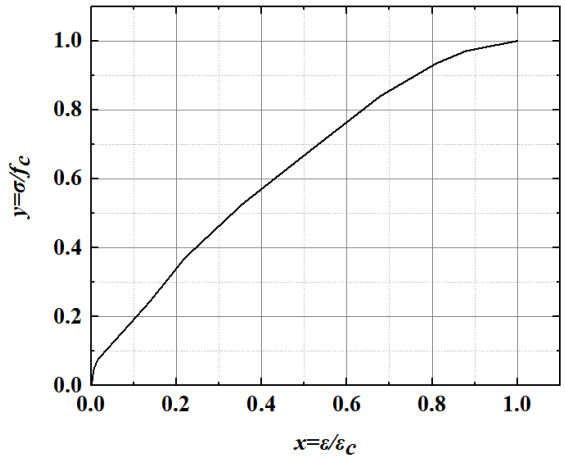

Figure 6: AASF-AFAAC compression σ-ε curve

3.2 Prediction of AASF-AFAAC Stress-Strain Relationship Model

To characterize the stress-strain relationship of AASF-AFAAC under compressive conditions, a constitutive model suitable for alkali-activated lightweight aggregate concrete properties must be selected. Given that the experimental data primarily consist of pre-peak rise segment curves, this study focuses on analyzing a representative model applicable to the ascending phase. Considering the mechanical properties of AASF-AFAAC materials, a polynomial model proposed by Professor Guo Zhenhai from Tsinghua University was adopted.

The polynomial form constitutive equation proposed by Professor Guo Zhenhai from Tsinghua University [27] is as follows:

$$y = a_0 + a_1 x + a_2 x^2 + a_3 x^3 \tag{1}$$

In the formulaa_0 , a_1 , a_2 a_3:, are undetermined coefficients, x=ε/ε0, y=σ/σ0 (where ε0 and σ0 represent peak strain and peak stress, respectively).

When x=0, y=0, we get:

$$a_0 = 0 \tag{2}$$

The initial tangent slope equals the ratio of elastic modulus to peak stress, i.e., =:$\frac{dy}{dx}|_{x=0}$ $\frac{E_c \cdot \varepsilon_0}{f_c}$

$$y'(0) = a_1 = \frac{E_c \cdot \varepsilon_0}{f_c} \tag{3}$$

When the strain reaches $\varepsilon_0 f_c$ its peak value, the stress attains its peak strength, i.e., y(1)=1.

$$a_1 + a_2 + a_3 = 1 \tag{4}$$

The tangent slope at the peak point is zero (where stress reaches its maximum value), i.e., y'(1) = 0:

$$a_1 + 2a_2 + 3a_3 = 0 \tag{5}$$

By setting up two equations, we obtain:

$$a_2 = 3 - 2a_1 \tag{6}$$

$$a_3 = a_1 - 2 \tag{7}$$

Substituting into Equation (20) yields:

$$a_0 = 0,\ a_2 = 3-2a_1, a_3 = a_1-2$$

$$y = a_1 x + (3\text{-}2a_1)\, x^2 + (a_1\text{-}2)\, x^3 \tag{8}$$

The average value prediction of AASF-AFAAC stress-strain curves was performed using Equation (8), with results shown in Figure 7. The model fitting parameters (a1) and correlation coefficient R^2 values are presented in Table 6. R^2 quantifies the correlation between predicted curves and experimental data: a higher R^2 value indicates stronger correlation and greater prediction accuracy. Results demonstrate that the predicted curves from the Guozhenhai model exhibit excellent agreement with experimental mean curves, low dispersion, and high stability. Therefore, this model is recommended as the prediction equation for AASF-AFAAC stress-strain relationships.

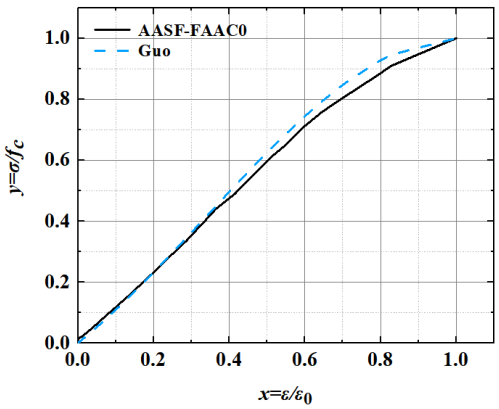

(a)AASF-AFAAC0

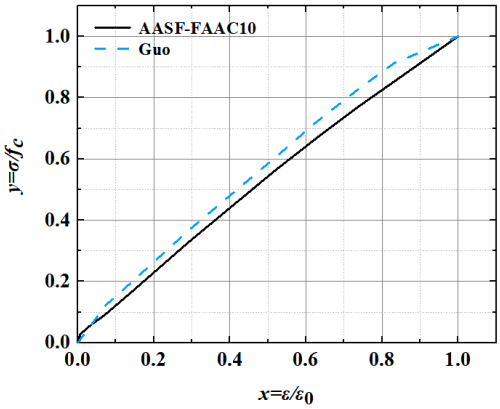

(b)AASF-AFAAC10

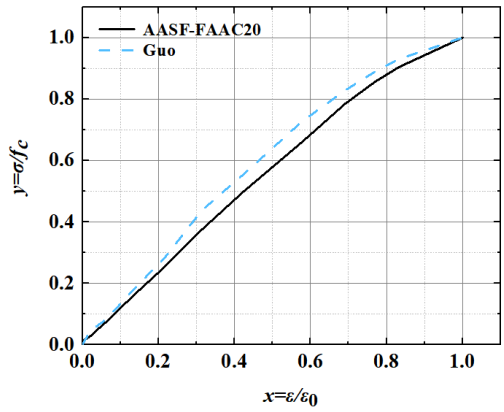

(c)AASF-AFAAC20

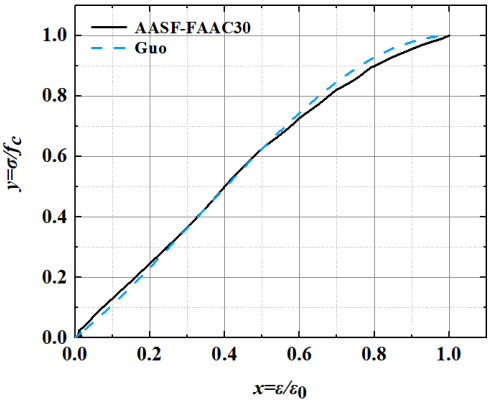

(d)AASF-AFAAC30

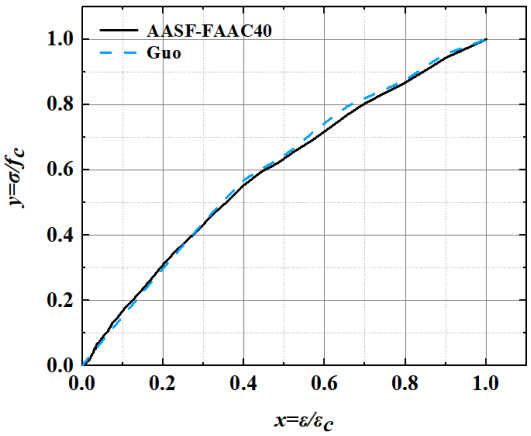

(e)AASF-AFAAC40

Figure 7: Comparison of stress-strain model predictions for AASF-AFAAC

Table 6: Model fitting parameters and correlation indicators

group	a_1	Pass through Guanzhou (R2)
AASF-FAAC0	1.00	0.9679
AASF-FAAC10	1.55	0.9077
AASF-FAAC20	2.05	0.8403
AASF-FAAC30	1.00	0.9757
AASF-FAAC40	1.51	0.9670
R2 mean value		0.9317

4. Conclusion

Based on the results of axial compression tests, a systematic analysis was conducted on the stress-strain relationship and peak deformation characteristics of AASF-AFAAC, followed by fitting studies of the test curves using multiple classical constitutive models. The main conclusions are as follows:

(1) The stress-strain curves of AASF-AFAAC under axial compression exhibit pronounced nonlinear characteristics, which can be divided into four distinct phases: compaction stage, elastic stage, elastoplastic stage, and post-peak softening stage. During initial loading, the material demonstrates pore compaction behavior, followed by rapid stress-strain increase. Upon reaching peak stress, the stress enters a gradual decline phase, reflecting ductile fracture characteristics.

(2) The dosage of fly ash has a certain impact on the peak compressive strain of concrete. With increasing fly ash dosage, the peak compressive strain generally exhibits a trend of first decreasing, then slightly recovering, and finally decreasing again. Appropriate fly ash dosage is beneficial for improving the matrix structure, whereas excessive dosage may weaken the overall deformation capacity of the material.

(3) Based on the normalized stress-strain curve, the test results were fitted and analyzed using the Guo-Zhenhai model. The results demonstrate that the Guo-Zhenhai model exhibits high fitting accuracy and can effectively describe the nonlinear mechanical behavior of AASF-AFAAC during compression.

In conclusion, the Zhenhai model can accurately reflect the stress-strain relationship of AASF-AFAAC, providing valuable references for subsequent structural analysis and engineering

applications.

References

[1] Puertas, F., Martínez-Ramírez, S., Alonso, S., et al. Alkali-activated fly ash/slag cements: Strength behaviour and hydration products[J]. Cement and Concrete Research, 2000, 30(10): 1625.

[2] Jiao, Z., Wang, Y., Zheng, W., et al. Effect of the activator on the performance of alkali-activated slag mortars with pottery sand as fine aggregate[J]. Construction and Building Materials, 2019, 197: 83.

[3] Annual Development Report of China's Sand and Gravel Aggregate Industry[R]. China Sand and Gravel Association 2024

[4] Association, C. I. a. S., Development Report of Comprehensive Utilization of Metallurgical Solid Waste Resources in 2022[S]. Metallurgical Industry Publishing House 2023

[5] Blanco, F., García, P., Mateos, P., et al. Characteristics and properties of lightweight concrete manufactured with cenospheres[J]. Cement and Concrete Research, 2000, 30 (11): 1715.

[6] Tiwari, V., Shukla, A., Bose, A. Acoustic properties of cenosphere reinforced cement and asphalt concrete[J]. Applied Acoustics, 2004, 65 (3): 263.

[7] Li, W., Jia, X., Ni, G., et al. Mechanical Properties of Fly Ash Ceramsite Concrete Produced in a Single-Cylinder Rotary Kiln[J]. Buildings (Basel), 2025, 15: 3124.

[8] Przychodzień, P., Katzer, J. Properties of Structural Lightweight Aggregate Concrete Based on Sintered Fly Ash and Modified with Exfoliated Vermiculite[J]. Materials, 2021, 14 (20):5922.

[9] Kayali, O., Haque, M. N., Zhu, B. Drying shrinkage of fibre-reinforced lightweight aggregate concrete containing fly ash[J]. Cement and Concrete Research, 1999, 29 (11): 1835.

[10] Domagała, L. Durability of Structural Lightweight Concrete with Sintered Fly Ash Aggregate[J]. Materials, 2020, 13 (20): 4565.

[11] Satpathy, H. P., Patel, S. K., Nayak, A. N. Development of sustainable lightweight concrete using fly ash cenosphere and sintered fly ash aggregate[J]. Construction and Building Materials, 2019, 202:636.

[12] Guo, J., Yuan, K., Xu, J., et al., The Workability and Mechanical Performance of Fly Ash Cenosphere–Desert Sand Ceramsite Concrete: An Experimental Study and Analysis[J]. Materials, (2023), Vol. 16, p 1298

[13] Guerrieri, M., Sanjayan, J. G. Behavior of combined fly ash/slag-based geopolymers when exposed to high temperatures[J]. Fire and Materials, 2010, 34 (4):163.

[14] Ismail, I., Bernal, S. A., Provis, J. L., et al. Microstructural changes in alkali activated fly ash/slag geopolymers with sulfate exposure[J]. Materials and Structures, 2013, 46 (3):361.

[15] IPCC. Climate Change 2023: The Physical Science Basis[R]. Cambridge University Press, 2023.

[16] Turner, L. K., Collins, F. G. Carbon dioxide equivalent (CO2-e) emissions: A comparison between geopolymer and OPC cement concrete[J]. Construction and Building Materials, 2013, 43:125.

[17] Abdalqader, A. F., Jin, F., Al-Tabbaa, A. Development of greener alkali-activated cement: utilisation of sodium carbonate for activating slag and fly ash mixtures[J]. Journal of Cleaner Production, 2016, 113:66.

[18] Amer, I., Kohail, M., El-Feky, M. S., et al. A review on alkali-activated slag concrete. Ain Shams Engineering Journal 2021 12 (2):1475.

[19] McLellan, B. C., Williams, R. P., Lay, J., et al. Costs and carbon emissions for geopolymer pastes in comparison to ordinary portland cement[J]. Journal of Cleaner Production 2011 19 (9):1080.

[20] Zhou, X., Zeng, Y., Chen, P., et al. Mechanical properties of basalt and polypropylene fibre-reinforced alkali-activated slag concrete[J]. Construction and Building Materials 2021 269:121284.

[21] Melo Neto, A. A., Cincotto, M. A., Repette, W. Drying and autogenous shrinkage of pastes and mortars with activated slag cement[J]. Cement and Concrete Research, 2008, 38 (4):565.

[22] Li, Z., Lu, T., Liang, X., et al. Mechanisms of autogenous shrinkage of alkali-activated slag and fly ash pastes[J]. Cement and Concrete Research, 2020, 135:106107.

[23] Bondar, D., Nanukuttan, S., Provis, J. L., et al. Efficient mix design of alkali activated slag concretes based on packing fraction of ingredients and paste thickness[J]. Journal of Cleaner Production, 2019, 218: 438.

[24] Li, N., Shi, C., Zhang, Z., et al. A mixture proportioning method for the development of performance-based alkali-activated slag-based concrete[J]. Cement & Concrete Composites, 2018, 93: 163.

[25] Ministry of Housing and Urban-Rural Development of the People's Republic of China. Design Code for Ordinary Concrete Mix Proportion (JGJ 55-2011) [S]. Beijing: China Architecture & Building Press, 2011.

[26] Ministry of Construction of the People's Republic of China. Technical Specification for Light Aggregate Concrete JGJ51-2002[S]. Beijing: China Architecture & Building Press, 2002.

[27] Guo Zhenhai. Principles of Reinforced Concrete (3rd Edition) [M]. Beijing: Tsinghua University Press, 2013.

[28] ACI Committee 318. Building Code Requirements for Structural Concrete and Commentary 318-19/318R-19[S].

ACI:2019.
[29] ACI Committee 318. Building Code Requirements for Structural Concrete and Commentary 318-08/318R-08[S]. ACI:2008.
[30] Tang, Zhuo et al. Uniaxial Compressive Behaviors of Fly Ash/Slag-Based Geopolymeric Concrete with Recycled Aggregates[J]. Cement & concrete composites, 2019, 104: 103375.
[31] Comité Euro-International du Béton & Fédération Internationale de la Précontrainte.. CEB-FIP Model Code, 1990, [S]. China Architecture & Building Press:1993.
[32] Ministry of Housing and Urban-Rural Development of the People's Republic of China. Technical Code for Light Aggregate Concrete Structures (JGJ12-2006) [S]. Beijing: China Architecture & Building Press, 2006.